ACS Energy LETTERS

http://pubs.acs.org/journal/aelccp

LETTER

Enhancing Charge Carrier Delocalization in Perovskite Quantum Dot Solids with Energetically Aligned Conjugated Capping Ligands

Evan T. Vickers, Emily E. Enlow, William G. Delmas, Albert C. DiBenedetto, Ashraful H. Chowdhury, Behzad Bahrami, Benjamin W. Dreskin, Thomas A. Graham, Isaak N. Hernandez, Sue A. Carter, Sayantani Ghosh, Qiquan Qiao, and Jin Z. Zhang*

Cite This: *ACS Energy Lett.* 2020, 5, 817–825

Read Online

ACCESS | Metrics & More | Article Recommendations | Supporting Information

ABSTRACT: **Compared to bulk perovskites, charge transport in perovskite quantum dot (PQD) solids is limited. To address this issue, energetically aligned capping ligands were used to prepare methylammonium lead bromide ($MAPbBr_3$) PQDs toward enhancing surface charge carrier density in PQD solids. Trans-cinnamic acid (TCA) and its derivates, functionalized with electron-donating or electron-withdrawing groups to modulate energy levels, are used as passivating exciton-delocalizing ligands (EDLs) to decrease the energy gap with respect to the PQD core. 3,3-Diphenylpropylamine (DPPA) ligand is shown to stabilize EDLs on the PQD surface through $\pi-\pi$ stacking intermolecular interaction, mitigating charge trapping and nonradiative decay. Passivation using EDLs in combination with DPPA increases the photoluminescence (PL) quantum yield (QY) (90%), photoconductivity, extraction, mobility, transport time, and lifetime of charge carriers in PQD solids. Prototype PQD-based light-emitting diodes (LEDs) were demonstrated with a low turn-on voltage of 2.5 V.**

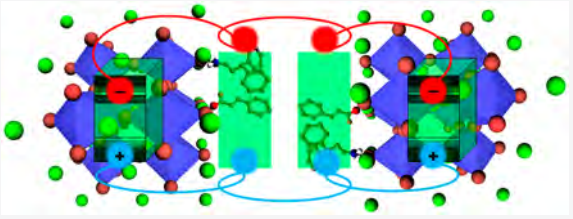

Semiconductor QDs based on organo-metal halide perovskites (OMHP) with the formula ABX_3 (A = methylammonium (MA^+), B = Pb^{2+}, X = Cl^-, Br^-, I^-) show great promise for optoelectronic applications because of their size-tunable bandgap, facile solution-based synthesis and potential low-cost fabrication.[1−9] Compared to other semiconductors, OMHPs show a high tolerance for defects and long exciton lifetimes, which enable fabrication of highly efficient devices.[10−17]

For device applications, such as photovoltaic (PV) or light-emitting diode (LED), electronic inter-PQD coupling is critical for effective charge transport through PQD solid film. However, this has been a major limiting factor since most ligands used to stabilize PQDs are insulating.[18] Such ligands present a large potential barrier for charge transfer between PQDs in solid film.[19−23] For example, $CsPbI_3$ PQDs synthesized with insulating oleylamine and oleic acid capping ligands were fabricated into solar cells with optimal PQD film thickness near 200 nm.[24] Films with greater thickness resulted in a decrease of performance mainly due to the lack of photocurrent and charge transport. The state-of-the-art perovskite solar cells based on bulk film have optimal film thicknesses between 400 and 800 nm.[25−28] Therefore, PQD films need to be thick enough for sufficient light absorption and, at the same time, maintain effective charge transport.

To improve charge transport, one approach is to incorporate conjugated capping ligands to enable delocalization of charge carriers from the QD to its ligands. This allows greater access of charge carriers at interfacial regions. In a previous report, using hole accepting aromatic ligands for CdSe QDs resulted in a 10-fold improvement in short circuit current density (I_{sc}) compared to passivating with long-chain hydrocarbon ligands.[29] This method was extended to the hole-delocalizing ligand phenyldithiocarbamate (PTC) for CdSe QDs.[30−33] Conjugating PTC to CdSe QDs causes a bathochromic shift in the absorption spectrum, which signifies an extension in charge carrier delocalization volume and follows the quantum confinement effect. This QD-ligand coupling is attributed to

Received: January 14, 2020
Accepted: February 12, 2020
Published: February 12, 2020

https://dx.doi.org/10.1021/acsenergylett.0c00093
ACS Energy Lett. 2020, 5, 817–825

energetic alignment between the highest occupied molecular orbitals (HOMO) of PTC and the highest density-of-states in the valence band-edge of CdSe QDs. In other studies, the effect of PbS QD surface modification on exciton delocalization was investigated using trans-cinnamic acid (TCA) derivatives as capping ligands.[34−36] Functionalizing the TCA molecule with electron-withdrawing or electron-donating groups profoundly affects the band-edge positions, bandgap, and optical absorption enhancement of PbS QDs. Furthermore, energetic alignment between the orbitals of exciton-delocalizing ligands (EDLs) and the band-edges of QDs can affect charge carrier cooling, which is sensitive to the ligand binding configuration.[37] Therefore, in addition to energetic alignment, specific EDL binding on the QD surface can significantly affect QD−QD electronic coupling and, thereby, charge transport in QD solids.

Using EDLs to increase QD−QD electronic coupling has also been reported for $MAPbBr_3$ PQDs. An LED device fabricated using $MAPbBr_3$ PQDs passivated with EDLs resulted in 22-fold higher conductivity and carrier mobility than $MAPbBr_3$ PQDs with long alkyl-chain capping ligands.[22] Additionally, in our previous work, $MAPbBr_3$ PQDs passivated with EDLs were observed to have higher conductivity and charge mobility along with longer excitonic recombination lifetime and faster charge transport time.[23] However, to achieve greater QD−QD electronic coupling for PQD solids, it is critical to energetically align the related molecular orbitals of the ligands with the band-edges of the PQD core.

In this work, $MAPbBr_3$ PQDs were synthesized by surface passivating with valeric acid (VA), TCA, *trans*-4-(trifluoromethyl) cinnamic acid (TFCA), *trans*-2,3,4,5,6-pentafluorocinnamic acid (PFCA), and *trans*-4-methoxycinnamic acid (MOCA) to vary their energy levels with respect to the band-edges of the PQD core, as well as butylamine (BTYA) and 3,3-diphenylpropylamine (DPPA), to stabilize the conjugated carboxylate ions or alter their binding geometry on the PQD surface. Optical and photoelectrochemical, as well as time-resolved optical and electrical measurements, have confirmed that conjugated ligands with HOMO or lowest unoccupied molecular orbital (LUMO) closest to the band-edges of the $MAPbBr_3$ PQDs increases charge delocalization on the PQD surface when passivated in combination with DPPA. DPPA's $\pi-\pi$ stacking intermolecular interaction in conjunction with TCA, TFCA, or MOCA, generates PQD solid films with enhanced optical and electronic properties, as well as produces bright electroluminescent LED devices with low turn-on voltages.

$MAPbBr_3$ PQDs were synthesized by following a previously reported procedure.[23] Precursor solution consisting of $PbBr_2$, MABr, DPPA, or BTYA and VA, TCA, TFCA, PFCA, or MOCA is dissolved in *N*,*N*-dimethylformamide (DMF) and rapidly injected into a vigorously stirred toluene antisolvent. A detailed description of the synthesis is in the Supporting Information (SI). Absolute PLQY data were obtained using an integrating sphere, a diagram of the measurement is displayed in Figure S1. Absolute PLQY for each $MAPbBr_3$ PQD sample is shown in Table 1. DPPA-TCA $MAPbBr_3$ PQDs are observed to have the highest absolute PLQY at 90%. Among the PQDs synthesized with BTYA, BTYA-MOCA $MAPbBr_3$ PQDs were observed to have the highest PLQY at 72%. The UV−vis absorption and photoluminescence (PL) spectra of each $MAPbBr_3$ PQD sample is displayed in Figure 1a and b. Each $MAPbBr_3$ PQD sample was tuned to have an exciton absorption peak between 510 and 525 nm and PL peak between 515 and 530 nm to accurately compare optical and electronic properties among different PQD samples.

Table 1. Absolute PLQY of $MAPbBr_3$ QDs and Molecular Structure of (a) TCA, (b) TFCA, (c) PFCA, (d) MOCA, (e) VA, (f) BTYA, and (g) DPPA

$MAPbBr_3$ PQD	PLQY(%)
BTYA-VA	18
BTYA-TCA	52
BTYA-TFCA	30
BTYA-PFCA	18
BTYA-MOCA	72
DPPA-VA	36
DPPA-TCA	90
DPPA-TFCA	46
DPPA-PFCA	46
DPPA-MOCA	58

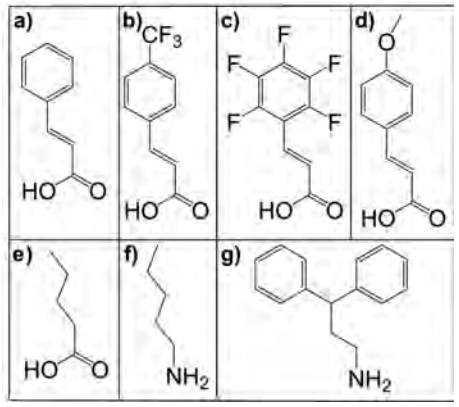

To determine the size and shape, high-resolution transmission electron microscopy (HRTEM) was performed, as shown in Figure 1c and d. The average diameter for the PQDs synthesized with BTYA and VA, TCA, TFCA, PFCA, or MOCA is 6.1 ± 1.5 nm, while PQDs synthesized with DPPA and each respective acid is slightly larger at 6.8 ± 1.3 nm. Shown in the inset of Figure 1c and d are images of lattice spacing, which is measured to be 0.29 nm for each $MAPbBr_3$ PQD sample, corresponding to the (002) crystal face of cubic $CH_3NH_3PbBr_3$.[38]

To confirm the presence of each capping ligand, Fourier transform-infrared (FT-IR) spectroscopy was conducted for each PQD sample, as shown in Figure S2. Monosubstituted aromatic C−H in the regions 770−730 and 720−680 cm^{-1} is observed for each $MAPbBr_3$ PQD, indicating the presence of TCA, TFCA, PFCA, or MOCA from each respective $MAPbBr_3$ PQD.

The extent of charge carrier delocalization from passivating with conjugated capping ligands was determined from a ligand exchange using $MAPbBr_3$ magic-sized clusters (MSCs) capped with BTYA and oleic acid (OA), as well as DPPA and OA. BTYA-OA and DPPA-OA $MAPbBr_3$ MSCs were synthesized following a previously reported procedure.[39] Detail of the synthesis is in SI. MSCs were chosen for ligand exchange because they are in a very strong confinement regime and more strongly confined charge carriers will have a greater sensitivity to increases to extra delocalization volume. The sizes of BTYA-

https://dx.doi.org/10.1021/acsenergylett.0c00093
ACS Energy Lett. 2020, 5, 817−825

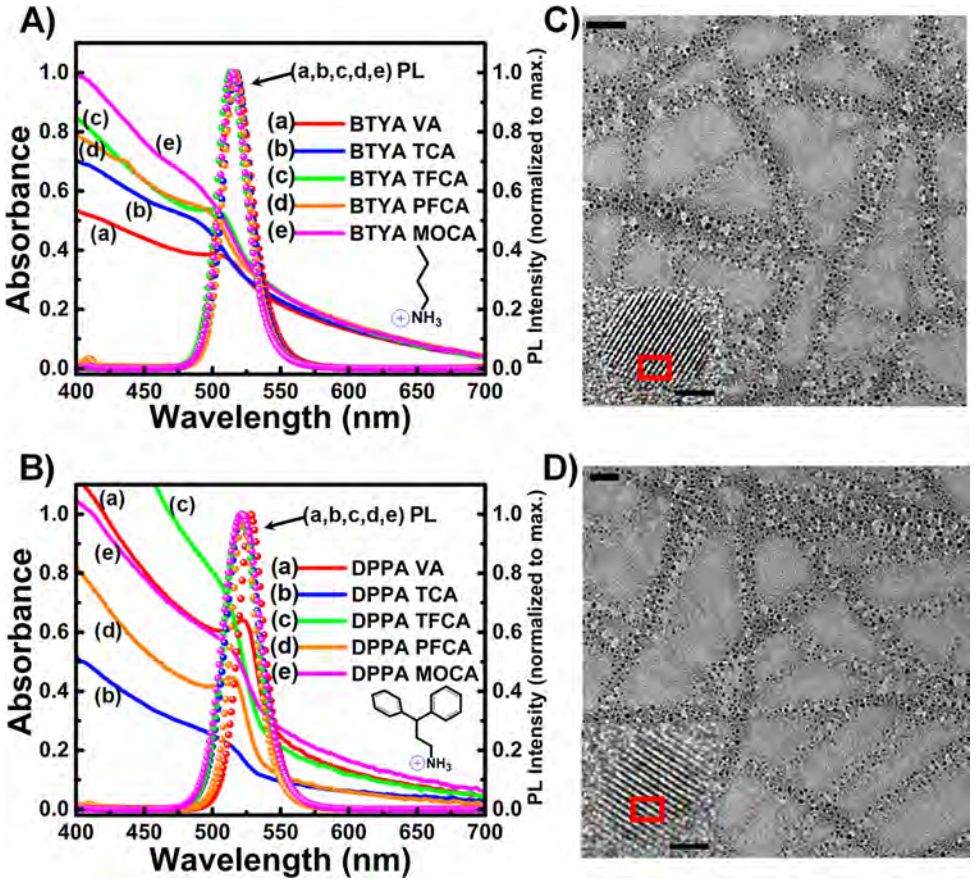

Figure 1. UV−vis absorption (solid line) and PL spectra (dotted line) of (A) BTYA-VA (a, red), -TCA (b, blue), -TFCA (c, green), -PFCA (d, orange), and -MOCA (e, magenta) and (B) DPPA-VA (a, red), -TCA (b, blue), -TFCA (c, green), -PFCA (d, orange), and -MOCA (e, magenta) $MAPbBr_3$ PQDs suspended in toluene. (C) HRTEM image of $MAPbBr_3$ PQDs passivated with DPPA-TCA (scale bar 10 nm). The lower left inset is image of lattice spacing (scale bar 2 nm). (D) HRTEM image of BTYA-TCA $MAPbBr_3$ PQDs (scale bar 10 nm), and the lower left inset is lattice spacing image (scale bar 2 nm). HRTEM images are similar with respect to BTYA or DPPA amine with each acid.

OA and DPPA-OA MSCs were estimated using the Brus equation developed for QDs.[40] Because of their molecular-like structures, TEM images of the MSCs could not be obtained.[39,41] These calculated values are used as estimates and may not reflect the true size. Detail of the calculation and ligand exchange procedure is in SI. Before ligand exchange with TCA, the BTYA-OA and DPPA-OA MSC sizes were calculated to be 2.89 and 2.65 nm, respectively. After exchanging OA ligands with TCA ligands, a 4 nm redshift in exciton absorption peak and 4 nm red-shift in PL peak was observed for the BTYA-TCA MSC solution, equivalent of an increase in size to 2.99 nm, as shown in Figure 2a. The delocalization radius was estimated by subtracting the calculated MSC size before and after ligand exchange.[31] On the basis of the bandgap shift, this corresponds to an increase in delocalization radius of 0.05 nm. For the DPPA-OA MSC solution, exchanging OA ligands for TCA ligands resulted in a 27 nm redshift of the absorption peak and 49 nm redshift in PL peak, as displayed in Figure 2b. This translates to a calculated size of 3.30 nm. Therefore, the increase in delocalization radius for DPPA-TCA MSC solution is calculated to be 0.33 nm. The larger increase in delocalization radius upon ligand exchange for the DPPA-OA MSC solution could be due to stabilization of the TCA ligands on the PQD surface from the $\pi-\pi$ stacking interactions between the aromatic rings in the DPPA and TCA molecules. This could enable more TCA molecules to adsorb to the PQD lattice or orient TCA to have more geometric orbital overlap.

Furthermore, the PLQY before and after ligand exchange was measured. Before ligand exchange the PLQY of BTYA-OA and DPPA-OA MSC solution was calculated to be 18 ± 4% and 12 ± 3% (vs quinine sulfate, 58%), respectively. After ligand exchange, the PLQY of BTYA-TCA and DPPA-TCA MSC solution was 11 ± 3% and 36 ± 5%, respectively. This enhancement in PLQY has been previously observed in CdSe QDs upon ligand exchange with an EDL, which can be attributed to stabilization of the excitonic state and increased probability of band-edge transitions.[33]

To determine the extent of ligand interaction with the PQD core, FT-IR spectroscopy was performed before and after ligand exchange. As shown in Figure 2c, the most noticeable changes in the FT-IR spectra for the BTYA-OA MSCs upon ligand exchange with TCA is the appearance of strong monosubstituted aromatic C−H at 773 and 688 cm^{-1}. In addition, a strong peak at 733 cm^{-1} and shoulder peak at 716 cm^{-1} appear in the FT-IR spectrum after ligand exchange, which may also be indicative of different bound states of the TCA ligand on the PQD lattice.[42−44] For the DPPA-OA MSC ligand exchange with TCA, due to the aromatic DPPA molecule, multiple aromatic C−H is observed before ligand exchange at 770, 750, 737, and 702 cm^{-1}, as shown in Figure 2d. After ligand exchange, peaks in this region become stronger in intensity, sharper, and slightly shifted. Peaks after ligand

https://dx.doi.org/10.1021/acsenergylett.0c00093
ACS Energy Lett. 2020, 5, 817−825

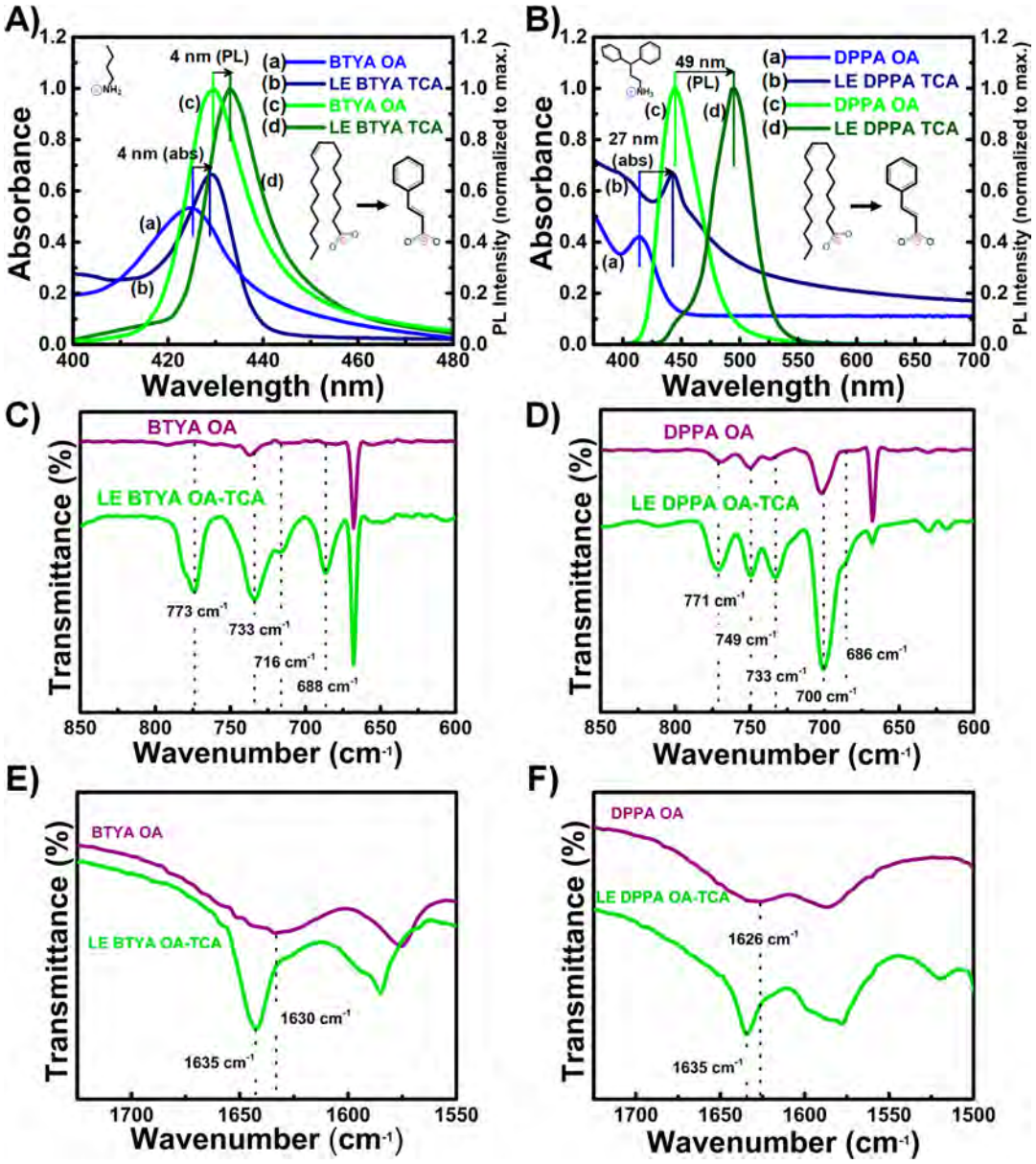

Figure 2. UV−vis absorption spectra of (A) BTYA-OA and (B) DPPA-OA MSCs before and after ligand exchange with TCA. FT-IR spectra of (C) BTYA-OA and (D) DPPA-OA MSCs before and after ligand exchange with TCA in the C-H aromatic region, and (E) BTYA-OA and (F) DPPA-OA MSCs before and after ligand exchange with TCA in the C═O stretching region.

exchange in the monosubstituted aromatic C−H region are at 771, 749, 733, and 700 cm^{-1}, as well as the appearance of a 686 cm^{-1} shoulder peak. Shown in Figure 2e and f is the C═O stretching before and after ligand exchange. Before ligand exchange for BTYA-OA and DPPA-OA MSCs, there is weak and broad C═O stretching at 1630 and 1626 cm^{-1}, respectively, corresponding to OA. After ligand exchange, these peaks disappear, and there is an appearance of a strong and sharp at peak 1635 cm^{-1} for both MSC solutions, which is assigned to the C═O stretching of TCA. Therefore, it may be concluded that TCA ligands significantly or completely replaced OA ligands.

The photogenerated charge carrier dynamics of each $MAPbBr_3$ PQD sample was investigated in solid films using time-correlated single-photon counting (TCSPC). Details of the measurements are described in SI. Comparing the valence band (VB) and conduction band (CB) edges of the PQD core with the HOMO and LUMO energy levels of each conjugated acid, based on calculations using density functional theory (DFT/B3LYP), as well as values from previous reports,[35,45,46] TCA's HOMO and LUMO orbitals are both near the VB and CB edges of the PQD core, while TFCA has LUMO more aligned to the CB edge and MOCA has its HOMO more aligned to the VB edge. The relevant energy levels are summarized in Figure S3. Therefore, TCA, TFCA, and MOCA are more likely to facilitate delocalization of photogenerated charge carriers in the PQD core than VA and PFCA. However, the strong interaction between the orbitals of EDLs and PQD core may facilitate trapping of charge carriers if the EDL is bound in a particular binding geometry.[37] On the surface of the PQD core, the intermolecular interaction of adjacent BTYA and EDL ligands is relatively weaker than the $\pi-\pi$ stacking intermolecular interaction between adjacent DPPA and EDL ligands. Because of the stronger $\pi-\pi$ stacking

https://dx.doi.org/10.1021/acsenergylett.0c00093
ACS Energy Lett. 2020, 5, 817−825

intermolecular interactions between adjacent DPPA and EDL ligands, vibration and rotation of the EDLs may be more restrained than with BTYA. Therefore, charge carriers delocalizing into EDLs may have less nonradiative recombination in the company of DPPA than BTYA. As shown in Figure 3a and b, this may contribute to the shorter or similar

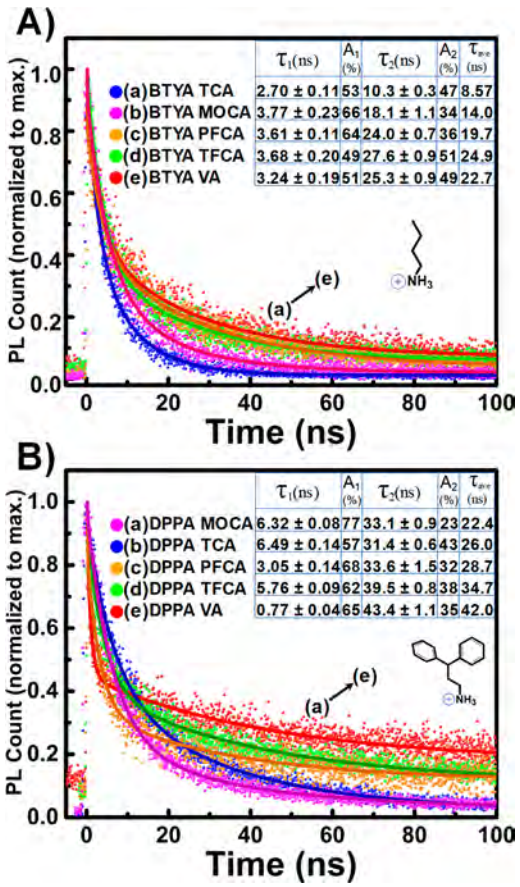

Figure 3. Time-resolved PL spectra of (A) BTYA-VA (e, red), -TCA (a, blue), -TFCA (d, green), -PFCA (c, orange), and -MOCA (b, magenta) and (B) DPPA-VA (e, red), -TCA (b, blue), -TFCA (d, green), -PFCA (c, orange), and -MOCA (a, magenta) MAPbBr3 PQD film on borosilicate glass substrate. Inset displays τ_1, τ_2, A_1, A_2, and τ_{ave} representing the fast and slow decay component lifetime and amplitude, and average PL lifetime, respectively.

PL lifetimes of BTYA-TCA, BTYA-TFCA, and BTYA-MOCA $MAPbBr_3$ PQD films compared to the PL lifetimes of BTYA-VA and BTYA-PFCA $MAPbBr_3$ PQD films, which contain insulating and not energetically aligned ligands, respectively. In contrast, significantly longer fast decay component lifetimes are observed in DPPA-TCA, DPPA-TFCA, DPPA-MOCA $MAPbBr_3$ PQD films, at 6.5 ± 0.1, 5.8 ± 0.1, and 6.3 ± 0.1 ns, respectively, compared to DPPA-VA and DPPA-PFCA $MAPbBr_3$ PQD film at 0.77 ± 0.04 and 3.05 ± 0.14 ns, respectively. This opposite trend from passivating with BTYA compared to DPPA may be due to DPPA's $\pi-\pi$ stacking interaction, which could restrict the molecular motion of the EDLs to a greater extent than BTYA. By restricting the molecular motion of the EDLs, a dampening of nonradiative pathways slow the rate of nonradiative recombination resulting in longer PL lifetime.

Using the absolute PLQY and the average PL lifetime, the radiative and nonradiative lifetimes were calculated. Detail of the calculation is included in SI. As shown in Table S1, coupling DPPA ligand with TCA or MOCA ligands enhances its radiative rate of decay with respect to its nonradiative rate. While for BTYA ligand, when coupled with EDLs, the radiative decay is comparable or significantly slower than its nonradiative decay. The increase in radiative decay rate and PLQY in DPPA passivated PQDs could be attributed to EDL's ability to stabilize photoexcited charge carriers generated in the PQD core by forming newly available interfacial states that could enhance the probability of band-edge transitions.[33] Whereas, for BTYA passivated PQDs, these interfacial states may trap charge carriers and increase nonradiative recombination.

To investigate the effect of EDLs on the conductivity and charge transport properties of PQD films, electrochemical impedance spectroscopy (EIS) was conducted. Details of the EIS measurements are supplied in SI. Figure 4a and b shows

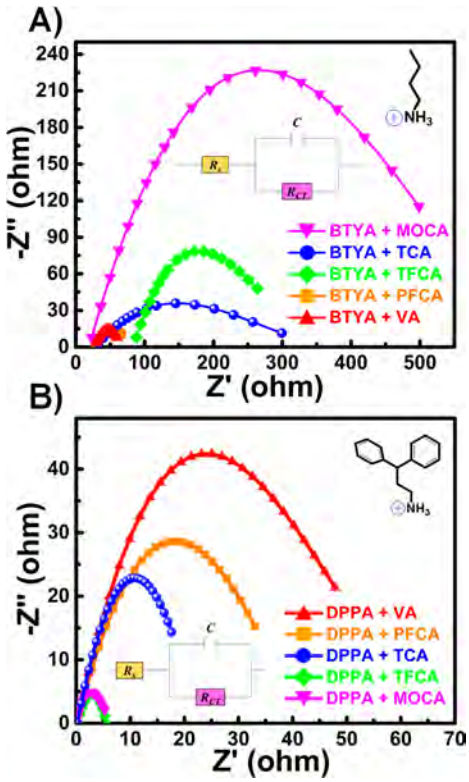

Figure 4. Nyquist spectra of (A) BTYA-VA, -TCA,-TFCA, -PFCA, and -MOCA and (B) DPPA-VA, -TCA, -TFCA, -PFCA, and -MOCA $MAPbBr_3$ PQD film on FTO substrate under one sun illumination (100 mW/cm^2). Inset displays equivalent circuit.

the Nyquist spectra of PQD films passivated with BTYA and DPPA with each acid, respectively. Table 2 provides a summary of the series resistance (R_s) and charge transport resistance (R_{CT}), determined by the first and second intercepts on the real axis, respectively, as well as the lifetime of charge transfer calculated using the constant-phase element (CPE) and R_{CT}.[47] The films containing DPPA passivated PQDs have consistent R_s near 0.195 ohm, while BTYA passivated PQD films have much larger R_s ranging from 30.1 to 78.8 ohm. However, the R_{CT} and τ_{rel} for BTYA-VA and DPPA-VA $MAPbBr_3$ PQD films is similar. Therefore, DPPA ligand by itself may not have significant conductivity advantages. The

https://dx.doi.org/10.1021/acsenergylett.0c00093
ACS Energy Lett. 2020, 5, 817−825

Table 2. Series Resistance (R_s), Charge Transport Resistance (R_{CT}), and Charge Transfer Lifetime (τ_{rel}) of Each $MAPbBr_3$ PQD Film on FTO Substrate

$MAPbBr_3$ PQD	R_s (ohm)	R_{CT} (ohm)	τ_{rel} (ms)
BTYA-VA	30.1	67.5	3.20
BTYA-TCA	33.0	341	16.1
BTYA-TFCA	78.8	328	15.5
BTYA-PFCA	30.1	80.8	3.83
BTYA-MOCA	30.1	645	30.5
DPPA-VA	0.195	60.5	2.97
DPPA-TCA	0.195	21.9	1.04
DPPA-TFCA	0.195	2.67	0.12
DPPA-PFCA	0.195	40.2	1.90
DPPA-MOCA	0.195	7.18	0.34

conjugated acids that are more energetically aligned with the PQD core; TCA, TFCA, and MOCA are observed to have the highest R_{CT} and slowest τ_{rel} for BTYA-passivated PQD films. This appears counterintuitive as the energetically aligned ligands should have strong PQD-ligand electronic coupling that increases surface charge carrier density. However, because of the instability and lack of $\pi-\pi$ stacking intermolecular interaction, the strong PQD-ligand coupling may enhance trapping of charge carriers and is consistent with the TRPL measurements. As observed in TRPL measurements, BTYA and DPPA capped PQDs have the opposite trend in EIS measurements. For DPPA-passivated PQDs, EDL-capped PQDs have the lowest R_{CT} and fastest τ_{rel}. The fastest τ_{rel} is measured to be 0.12 ms for DPPA-TFCA $MAPbBr_3$ PQD film. Our previous work using benzylamine (BZA) and benzoic acid (BA) delocalizing ligands have a τ_{rel} of 0.63 ms,[23] which is more than five times the lifetime of DPPA-TFCA $MAPbBr_3$ PQD film. Therefore, energy level alignment, as well as surface stabilization between the EDL and the PQD core, is crucial for increasing surface charge carrier density and charge transport in PQD solid film.

To examine the photogenerated current density, the transient photocurrent response ($I-t$ curve) was measured for each PQD solid film. Details of the measurements are in SI. As shown in Figure S4, the photogenerated current density measurements are consistent with the TRPL and EIS measurements. PQDs passivated with BTYA and the most energetically aligned ligands TCA, TFCA, and MOCA produce less photocurrent density than the VA and PFCA ligand, while the opposite is observed for DPPA passivated PQDs. Therefore, when the average ligand binding geometry facilitates charge trapping, the EDL diminishes photocurrent

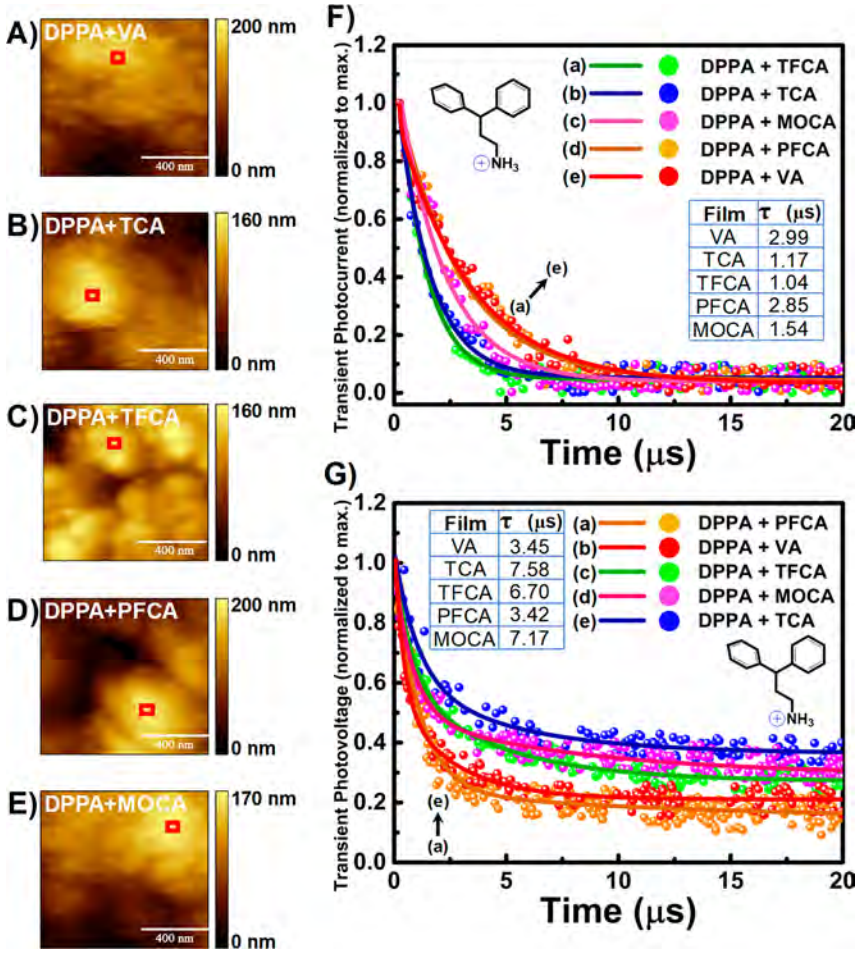

Figure 5. AFM topography images of (A) DPPA-VA, (B) DPPA-TCA, (C) DPPA-TFCA, (D) DPPA-PFCA, and (E) DPPA-MOCA $MAPbBr_3$ PQD films on FTO substrate. The area in the red square is where films were measured for TPC and TPV. (F) TPC decay curves of DPPA-VA (e, red), -TCA (b, blue), -TFCA (a, green), -PFCA (d, orange), and -MOCA (c, magenta) MAPbBr3 PQD films. (G) TPV decay curves of DPPA-VA (b, red), -TCA (e, blue), -TFCA (c, green), -PFCA (a, orange), and -MOCA (d, magenta) $MAPbBr_3$ PQD films.

https://dx.doi.org/10.1021/acsenergylett.0c00093
ACS Energy Lett. 2020, 5, 817−825

density even further than using an insulating capping ligand, such as VA.

To gain further insight into the effect of passivating PQDs with DPPA and EDLs, local transient photocurrent (TPC) and transient photovoltage (TPV) decay measurements were conducted using conductive atomic force microscopy (AFM). Details of the TPC and TPV measurements are supplied in SI. Shown in Figure 5a−e are AFM topography images of each PQD film that contain a red square representing an area 100 × 100 nm^2, where TPC and TPV measurements were performed with similar PQD film thickness on FTO substrate. Displayed in Figure 5f is the TPC decay curves, and the inset shows the charge transport times of each PQD film. This measurement is directly related to the conductivity and charge mobility of the PQD solid films. As shown, the PQDs passivated with energetically aligned ligands are observed to have up to 3-fold faster charge transport time than PQDs capped with insulating or not energetically aligned ligands. Our previous study of BZA-BA $MAPbBr_3$ PQD film was measured to have a charge transport time of 1.52 μs.[23] Thus, our new PQD films with dual passivation using energetically aligned and $\pi-\pi$ stacking ligands, outperform PQD film with insulating or not energetically aligned ligands, as well as our previously measured BZA-BA $MAPbBr_3$ PQD film.

TPV decays were collected to determine the charge carrier recombination lifetime of PQDs passivated with DPPA and each acid. Longer lifetimes represent a slower rate of exciton recombination and, hence, a greater probability of charge extraction. Shown in Figure 5g is the TPV decay curves and in the inset is the calculated charge carrier lifetimes. Dual passivation with EDLs and DPPA increases the charge carrier lifetime by two-folds with respective to using insulating or not energetically aligned ligands. Compared to 2.92 μs for BZA-BA $MAPbBr_3$ PQD film from our previous work,[23] the energetically aligned capping ligands coupled with DPPA shows major improvement in charge carrier lifetime.

To demonstrate applications of the $MAPbBr_3$ PQDs, DPPA-TCA and DPPA-VA PQD-based LEDs were constructed and successfully demonstrated in the configuration ITO/TiO_2/PQD/Spiro-MeOTAD/Au in a preliminary study. Details of the LED fabrication are in the SI. As shown from the current density−voltage ($J-V$) curve in Figure S5, DPPA-TCA $MAPbBr_3$ PQD-based LEDs generate much higher current density upon increasing voltage than DPPA-VA $MAPbBr_3$ PQD-based LEDs. DPPA-VA $MAPbBr_3$ PQD-based LEDs did not light up during the measurement; however, the DPPA-TCA $MAPbBr_3$ PQD-based LED generated bright electroluminescence (EL) with a turn-on voltage of 2.5 V. A representative EL spectrum is shown in Figure S6. $MAPbBr_3$ PQD-based LEDs with octylamine and oleic acid capping ligands have been recently reported to have turn-on voltages between 2.9 and 4.0 V.[48−50] Therefore, DPPA-TCA $MAPbBr_3$ PQD-based LEDs show enhanced performance.

In summary, we report the synthesis and characterization of $MAPbBr_3$ PQDs using a combination of capping ligands that are energetically aligned and stabilized by $\pi-\pi$ stacking. This results in higher PLQY, conductivity, and photocurrent density, as well as longer PL lifetime of charge carriers compared to PQDs with insulating ligands or EDLs not stabilized on the PQD surface. In addition, DPPA passivation increases PQD's charge carrier delocalization radius by more than 6-fold compared to BTYA passivation, as determined in TCA ligand exchange with OA. Furthermore, TPC and TPV measurements confirm faster charge transport times and longer charge carrier lifetimes, respectively, for PQDs passivated with EDLs. In addition, DPPA-TCA $MAPbBr_3$ PQD-based LEDs are observed to have better performance than DPPA-VA $MAPbBr_3$ PQD-based LEDs with a low turn-on voltage of 2.5 V. This work has demonstrated that energetically aligned conjugated capping ligands coupled with a spatial orbital overlap facilitator can significantly increase surface charge carrier density for improving optical and electrical properties of PQD films for potential optoelectronic device applications.

■ ASSOCIATED CONTENT

Supporting Information

The Supporting Information is available free of charge at https://pubs.acs.org/doi/10.1021/acsenergylett.0c00093.

Experimental section and supplementary figures (PDF)

■ AUTHOR INFORMATION

Corresponding Author

Jin Z. Zhang − *Department of Chemistry and Biochemistry, University of California, Santa Cruz, California 95064, United States;* orcid.org/0000-0003-3437-912X; Email: zhang@ucsc.edu

Authors

Evan T. Vickers − *Department of Chemistry and Biochemistry, University of California, Santa Cruz, California 95064, United States;* orcid.org/0000-0002-9594-4279

Emily E. Enlow − *Department of Physics, University of California, Santa Cruz, California 95064, United States*

William G. Delmas − *Department of Physics, School of Natural Sciences, University of California, Merced, California 95344, United States*

Albert C. DiBenedetto − *Department of Physics, School of Natural Sciences, University of California, Merced, California 95344, United States*

Ashraful H. Chowdhury − *Department of Electrical Engineering and Computer Science, Center for Advanced Photovoltaics and Sustainable Energy, South Dakota State University, Brookings, South Dakota 57007, United States*

Behzad Bahrami − *Department of Electrical Engineering and Computer Science, Center for Advanced Photovoltaics and Sustainable Energy, South Dakota State University, Brookings, South Dakota 57007, United States*

Benjamin W. Dreskin − *Department of Chemistry and Biochemistry, University of California, Santa Cruz, California 95064, United States*

Thomas A. Graham − *Department of Chemistry and Biochemistry, University of California, Santa Cruz, California 95064, United States*

Isaak N. Hernandez − *Department of Physics, School of Natural Sciences, University of California, Merced, California 95344, United States; Department of Physics, Massachusetts Institute of Technology, Cambridge, Massachusetts 02139, United States*

Sue A. Carter − *Department of Physics, University of California, Santa Cruz, California 95064, United States*

Sayantani Ghosh − *Department of Physics, School of Natural Sciences, University of California, Merced, California 95344, United States;* orcid.org/0000-0003-3440-7194

Qiquan Qiao − *Department of Electrical Engineering and Computer Science, Center for Advanced Photovoltaics and*

https://dx.doi.org/10.1021/acsenergylett.0c00093
ACS Energy Lett. 2020, 5, 817−825

Sustainable Energy, South Dakota State University, Brookings, South Dakota 57007, United States; orcid.org/0000-0002-4555-7887

Complete contact information is available at: https://pubs.acs.org/10.1021/acsenergylett.0c00093

Notes

This work is derived from the Subject Data supported in whole or part by NAS and USAID, and any opinions, findings, conclusions, or recommendations expressed in the paper are those of the authors alone and do not necessarily reflect the views of USAID or NAS.

The authors declare no competing financial interest.

■ ACKNOWLEDGMENTS

This research was supported by NASA through MACES (NNX15AQ01A), the NSF (CHE-1904547), and UCSC Committee on Research Special Research Grant. Work at the Molecular Foundry was supported by the Office of Science, Office of Basic Energy Sciences, of the U.S. Department of Energy under Contract DE-AC02-05CH11231. We acknowledge Dr. Tom Yuzvinsky for assistance with sample preparation and electron microscopy and the W.M. Keck Center for Nanoscale Optofluidics for use of the FEI Quanta 3D Dual beam microscope. Q.Q. acknowledges NSF MRI (1428992), NASA EPSCoR (NNX15AM83A), U.S.−Egypt Science and Technology (S&T) Joint Fund, SDBoR R&D Program and EDA University Center Program (ED18DEN3030025). We would like to thank Dr. Brian Moore for assisting us with high performance computing facility at South Dakota State University.

■ REFERENCES

(1) Sharenko, A.; Toney, M. F. Relationships between Lead Halide Perovskite Thin-Film Fabrication, Morphology, and Performance in Solar Cells. *J. Am. Chem. Soc.* **2016**, *138*, 463−470.

(2) Manser, J. S.; Christians, J. A.; Kamat, P. V. Intriguing Optoelectronic Properties of Metal Halide Perovskites. *Chem. Rev.* **2016**, *116*, 12956−13008.

(3) Snaith, H. J. Present Status and Future Prospects of Perovskite Photovoltaics. *Nat. Mater.* **2018**, *17*, 372−376.

(4) Shi, Z.; Jayatissa, A. H. Perovskite-Based Solar Cells: A Review of Recent Progress, Materials and Processing Methods. *Materials* **2018**, *11*, 729.

(5) Mohd Yusoff, A. R. B.; Gao, P.; Nazeeruddin, M. K. Recent Progress in Organohalide Lead Perovskites for Photovoltaic and Optoelectronic Applications. *Coord. Chem. Rev.* **2018**, *373*, 258−294.

(6) Sun, J.; Wu, J.; Tong, X.; Lin, F.; Wang, Y.; Wang, Z. M. Organic/Inorganic Metal Halide Perovskite Optoelectronic Devices Beyond Solar Cells. *Adv. Sci.* **2018**, *5*, 1700780.

(7) Park, M.-H.; Kim, J. S.; Heo, J.-M.; Ahn, S.; Jeong, S.-H.; Lee, T.-W. Boosting Efficiency in Polycrystalline Metal Halide Perovskite Light-Emitting Diodes. *ACS Energy Lett.* **2019**, *4*, 1134−1149.

(8) Wei, Z.; Xing, J. The Rise of Perovskite Light-Emitting Diodes. *J. Phys. Chem. Lett.* **2019**, *10*, 3035−3042.

(9) Pham, H. D.; Xianqiang, L.; Li, W.; Manzhos, S.; Kyaw, A. K. K.; Sonar, P. Organic Interfacial Materials for Perovskite-Based Optoelectronic Devices. *Energy Environ. Sci.* **2019**, *12*, 1177.

(10) Zhumekenov, A. A.; Saidaminov, M. I.; Haque, M. A.; Alarousu, E.; Sarmah, S. P.; Murali, B.; Dursun, I. D.; Miao, X.-H.; Abdelhady, A. L.; Wu, T.; et al. Formamidinium Lead Halide Perovskite Crystals with Unprecedented Long Carrier Dynamics and Diffusion Length. *ACS Energy Lett.* **2016**, *1*, 32−37.

(11) Xu, W.; McLeod, J. A.; Yang, Y.; Wang, Y.; Wu, Z.; Bai, S.; Yuan, Z.; Song, T.; Wang, Y.; et al. Iodomethane-Mediated Organometal Halide Perovskite with Record Photoluminescence Lifetime. *ACS Appl. Mater. Interfaces* **2016**, *8*, 23181−23189.

(12) Steirer, K. X.; Schulz, P.; Teeter, G.; Stevanovic, V.; Yang, M.; Zhu, K.; Berry, J. J. Defect Tolerance in Methylammonium Lead Triiodide Perovskite. *ACS Energy Lett.* **2016**, *1*, 360−366.

(13) Kang, J.; Wang, L.-W. High Defect Tolerance in Lead Halide Perovskite $CsPbBr_3$. *J. Phys. Chem. Lett.* **2017**, *8*, 489−493.

(14) Huang, H.; Bodnarchuk, M. I.; Kershaw, S. V.; Kovalenko, M. V.; Rogach, A. L. Lead Halide Perovskite Nanocrystals in the Research Spotlight: Stability and Defect Tolerance. *ACS Energy Lett.* **2017**, *2*, 2071−2083.

(15) Meng, G.; Shi, Y.; Wang, X.; Wang, W.; Wang, S.; Ji, M.; Hao, C. New Insight into the Ultra-Long Lifetime of Excitons in Organic-Inorganic Perovskite: Reverse Intersystem Crossing. *J. Energy Chem.* **2018**, *27*, 1496−1500.

(16) Li, M.; Begum, R.; Fu, J.; Xu, Q.; Koh, T. M.; Veldhuis, S. A.; Grätzel, M.; Mathews, N.; Mhaisalkar, S.; Sum, T. C. Low Threshold and Efficient Multiple Exciton Generation in Halide Perovskite Nanocrystals. *Nat. Commun.* **2018**, *9*, 4197.

(17) Jena, A. K.; Kulkarni, A.; Miyasaka, T. Halide Perovskite Photovoltaics: Background, Status, and Future Prospects. *Chem. Rev.* **2019**, *119*, 3036−3103.

(18) Murray, C. B.; Kagan, C. R. Charge Transport in Strongly Coupled Quantum Dot Solids. *Nat. Nanotechnol.* **2015**, *10*, 1013−1026.

(19) Hines, D. A.; Kamat, P. V. Quantum Dot Surface Chemistry: Ligand Effects and Electron Transfer Reactions. *J. Phys. Chem. C* **2013**, *117*, 14418−14426.

(20) Hines, D. A.; Kamat, P. V. Recent Advances in Quantum Dot Surface Chemistry. *ACS Appl. Mater. Interfaces* **2014**, *6*, 3041−3057.

(21) Hoffman, J. B.; Alam, R.; Kamat, P. V. Why Surface Chemistry Matters for QD−QD Resonance Energy Transfer. *ACS Energy Lett.* **2017**, *2*, 391−396.

(22) Dai, J.; Xi, J.; Li, L.; Zhao, J.; Shi, Y.; Zhang, W.; Ran, C.; Jiao, B.; Hou, X.; Duan, X.; et al. Charge Transport between Coupling Colloidal Perovskite Quantum Dots Assisted by Functional Conjugated Ligands. *Angew. Chem., Int. Ed.* **2018**, *57*, 5754−5758.

(23) Vickers, E. T.; Graham, T. A.; Chowdhury, A. H.; Bahrami, B.; Dreskin, B. W.; Lindley, S.; Naghadeh, S. B.; Qiao, Q.; Zhang, J. Z. Improving Charge Carrier Delocalization in Perovskite Quantum Dots by Surface Passivation with Conductive Aromatic Ligands. *ACS Energy Lett.* **2018**, *3*, 2931−2939.

(24) Zolfaghari, Z.; Hassanabadi, E.; Pitarch-Tena, D.; Yoon, S. J.; Shariatinia, Z.; van de Lagemaat, J.; Luther, J. M.; Mora-Seró, I. Operation Mechanism of Perovskite Quantum Dot Solar Cells Probed by Impedance Spectroscopy. *ACS Energy Lett.* **2019**, *4*, 251−258.

(25) Liu, D.; Gangishetty, M. K.; Kelly, T. L. Effect of $CH_3NH_3PbI_3$ Thickness on Device Efficiency in Planar Heterojunction Perovskite Solar Cells. *J. Mater. Chem. A* **2014**, *2*, 19873−19881.

(26) Saliba, M.; Matsui, T.; Seo, J.-Y.; Domanski, K.; Correa-Baena, J. P.; Nazeeruddin, M. K.; Zakeeruddin, S. M.; Tress, W.; Abate, A.; Hagfeldt, A.; et al. Cesium-Containing Triple Cation Perovskite Solar Cells: Improved Stability, Reproducibility and High Efficiency. *Energy Environ. Sci.* **2016**, *9*, 1989−1997.

(27) Habisreutinger, S. N.; Wenger, B.; Snaith, H. J.; Nicholas, R. J. Dopant-Free Planar n-i-p Perovskite Solar Cells with Steady-State Efficiencies Exceeding 18%. *ACS Energy Lett.* **2017**, *2*, 622−628.

(28) Gao, L.; Spanopoulos, I.; Ke, W.; Huang, S.; Hadar, I.; Chen, L.; Li, X.; Yang, G.; Kanatzidis, M. G. Improved Environmental Stability and Solar Cell Efficiency of $(MA,FA)PbI_3$ Perovskite Using a Wide-Band-Gap 1D Thiazolium Lead Iodide Capping Layer Strategy. *ACS Energy Lett.* **2019**, *4*, 1763−1769.

(29) Liu, I.-S.; Lo, H.-H.; Chien, C.-T.; Lin, Y.-Y.; Chen, C.-W.; Chen, Y.-F.; Su, W.-F.; Liou, S.-C. Enhancing Photoluminescence Quenching and Photoelectric Properties of CdSe Quantum Dots with Hole Accepting Ligands. *J. Mater. Chem.* **2008**, *18*, 675−682.

(30) Frederick, M. T.; Weiss, E. A. Relaxation of Exciton Confinement in CdSe Quantum Dots by Modification with a Conjugated Dithiocarbamate Ligand. *ACS Nano* **2010**, *4*, 3195−3200.

(31) Frederick, M. T.; Amin, V. A.; Swenson, N. K.; Ho, A. Y.; Weiss, E. A. Control of Exciton Confinement in Quantum Dot-Organic Complexes through Energetic Alignment on Interfacial Orbitals. *Nano Lett.* **2013**, *13*, 287−292.
(32) Frederick, M. T.; Amin, V. A.; Weiss, E. A. Optical Properties of Strongly Coupled Quantum Dot-Ligand Systems. *J. Phys. Chem. Lett.* **2013**, *4*, 634−640.
(33) Jin, S.; Harris, R. D.; Lau, B.; Aruda, K. O.; Amin, V. A.; Weiss, E. A. Enhanced Rate of Radiative Decay in CdSe Quantum Dots upon Adsorption of an Exciton-Delocalizing Ligand. *Nano Lett.* **2014**, *14*, 5323−5328.
(34) Kroupa, D. M.; Vörös, M.; Brawand, N. P.; McNichols, B. W.; Miller, E. M.; Gu, J.; Nozik, A. J.; Sellinger, A.; Galli, G.; Beard, M. C. Tuning Colloidal Quantum Dot Band Edge Positions through Solution-Phase Surface Chemistry Modification. *Nat. Commun.* **2017**, *8*, 15257.
(35) Kroupa, D. M.; Vörös, M.; Brawand, N. P.; Bronstein, N.; McNichols, B. W.; Castaneda, C. V.; Nozik, A. J.; Sellinger, A.; Galli, G.; Beard, M. C. Optical Absorbance Enhancement in PbS QD/Cinnamate Ligand Complexes. *J. Phys. Chem. Lett.* **2018**, *9*, 3425−3433.
(36) Bronstein, N. D.; Martinez, M. S.; Kroupa, D. M.; Vörös, M.; Lu, H.; Brawand, N. P.; Nozik, A. J.; Sellinger, A.; Galli, G.; Beard, M. C. Designing Janus Ligand Shells on PbS Quantum Dots using Ligand-Ligand Cooperativity. *ACS Nano* **2019**, *13*, 3839−3846.
(37) Azzaro, M. S.; Babin, M. C.; Stauffer, S. K.; Henkelman, G.; Roberts, S. T. Can Exciton-Delocalizing Ligands Facilitate Hot Hole Transfer from Semiconductor Nanocrystals? *J. Phys. Chem. C* **2016**, *120*, 28224−28234.
(38) Schmidt, L. C.; Pertegas, A.; Gonzalez-Carrero, S.; Malinkiewicz, O.; Agouram, S.; Minguez Espallargas, G.; Bolink, H. J.; Galian, R. E.; Perez-Prieto, J. Nontemplate Synthesis of $CH_3NH_3PbBr_3$ Perovskite Nanoparticles. *J. Am. Chem. Soc.* **2014**, *136*, 850−853.
(39) Vickers, E. T.; Xu, K.; Dreskin, B. W.; Graham, T. A.; Li, X.; Zhang, J. Z. Ligand Dependent Growth and Optical Properties of Hybrid Organo-Metal Halide Perovskite Magic Sized Clusters. *J. Phys. Chem. C* **2019**, *123*, 18746−18752.
(40) Brus, L. E. Electron−electron and Electron-hole Interactions in Small Semiconductor Crystallites: The Size Dependence of the Lowest Excited Electronic State. *J. Chem. Phys.* **1984**, *80*, 4403−4409.
(41) Peng, L.; Dutta, A.; Xie, R.; Yang, W.; Pradhan, N. Dot-Wire-Platelet-Cube: Step Growth and Structural Transformations in $CsPbBr_3$ Perovskite Nanocrystals. *ACS Energy Lett.* **2018**, *3*, 2014−2020.
(42) Cooper, J. K.; Franco, A. M.; Gul, S.; Corrado, C.; Zhang, J. Z. Characterization of Primary Amine Capped CdSe, ZnSe, and ZnS Quantum Dots by FT-IR: Determination of Surface Bonding Interaction and Identification of Selective Desorption. *Langmuir* **2011**, *27*, 8486−8493.
(43) Son, J. G.; Choi, E.; Piao, Y.; Han, S. W.; Lee, T. G. Probing Organic Ligands and their Binding Schemes on Nanocrystals by Mass Spectrometric and FT-IR Spectroscopic Imaging. *Nanoscale* **2016**, *8*, 4573−4578.
(44) Peters, J. L.; van den Bos, K. H. W.; Van Aert, S.; Goris, B.; Bals, S.; Vanmaekelbergh, D. Ligand-Induced Shape Transformation of PbSe Nanocrystals. *Chem. Mater.* **2017**, *29*, 4122−4128.
(45) Leyden, M. R.; Meng, L.; Jiang, Y.; Ono, L. K.; Qiu, L.; Juarez-Perez, E. J.; Qin, C.; Adachi, C.; Qi, Y. Methylammonium Lead Bromide Perovskite Light-Emitting Diodes by Chemical Vapor Deposition. *J. Phys. Chem. Lett.* **2017**, *8*, 3193−3198.
(46) Sert, Y.; Doğan, H.; Navarrete, A.; Somanathan, R.; Aguirre, G.; Çırak, Ç. Experimental FT-IR, Laser-Raman and DFT Spectroscopic Analysis of 2,3,4,5,6-Pentafluoro-trans-cinnamic Acid. *Spectrochim. Acta, Part A* **2014**, *128*, 119−126.
(47) Kim, Y. C.; Kim, K. H.; Son, D.-Y.; Jeong, D.-N.; Seo, J.-Y.; Choi, Y. S.; Han, I. T.; Lee, S. Y.; Park, N. G. Printable Organometallic Perovskite Enables Large-area, Low-dose X-ray Imaging. *Nature* **2017**, *550*, 87−91.
(48) Jin, X.; Zhang, X.; Fang, H.; Deng, W.; Xu, X.; Jie, J.; Zhang, X. Facile Assembly of High-Quality Organic-Inorganic Hybrid Perovskite Quantum Dot Thin Films for Bright Light-Emitting Diodes. *Adv. Funct. Mater.* **2018**, *28*, 1705189.
(49) Yao, Y.; Yu, H.; Wu, Y.; Lu, Y.; Liu, Z.; Xu, X.; Ma, B.; Zhang, Q.; Chen, S.; Huang, W. Efficient Quantum Dot Light-Emitting Diodes Based on Trioctylphosphine Oxide-Passivated Organometallic Halide Perovskites. *ACS Omega* **2019**, *4*, 9150−9159.
(50) Huang, H.; Zhao, F.; Liu, L.; Zhang, F.; Wu, X.; Shi, L.; Zou, B.; Pei, Q.; Zhong, H. Emulsion Synthesis of Size-Tunable $CH_3NH_3PbBr_3$ Quantum Dots: An Alternative Route toward Efficient Light-Emitting Diodes. *ACS Appl. Mater. Interfaces* **2015**, *7*, 28128−28133.

https://dx.doi.org/10.1021/acsenergylett.0c00093
ACS Energy Lett. 2020, 5, 817−825